NANO LETTERS

pubs.acs.org/NanoLett Letter

Multiplex Ultrasound Imaging of Perfluorocarbon Nanodroplets Enabled by Decomposition of Postvaporization Dynamics

Austin Van Namen, Sidhartha Jandhyala, Catalina-Paula Spatarelu, Kenneth M. Tichauer, Kimberley S. Samkoe, and Geoffrey P. Luke*

Cite This: https://doi.org/10.1021/acs.nanolett.3c03719 Read Online

ACCESS | Metrics & More | Article Recommendations | Supporting Information

ABSTRACT: Despite the real-time, nonionizing, and cost-effective nature of ultrasound imaging, there is a dearth of methods to visualize two or more populations of contrast agents simultaneously—a technique known as multiplex imaging. Here, we present a new approach to multiplex ultrasound imaging using perfluorocarbon (PFC) nanodroplets. The nanodroplets, which undergo a liquid-to-gas phase transition in response to an acoustic trigger, act as activatable contrast agents. This work characterized the dynamic responses of two PFC nanodroplets with boiling points of 28 and 56 °C. These characteristic responses were then used to demonstrate that the relative concentrations of the two populations of PFC nanodroplets could be accurately measured in the same imaging volume within an average error of 1.1%. Overall, the findings indicate the potential of this approach for multiplex ultrasound imaging, allowing for the simultaneous visualization of multiple molecular targets simultaneously.

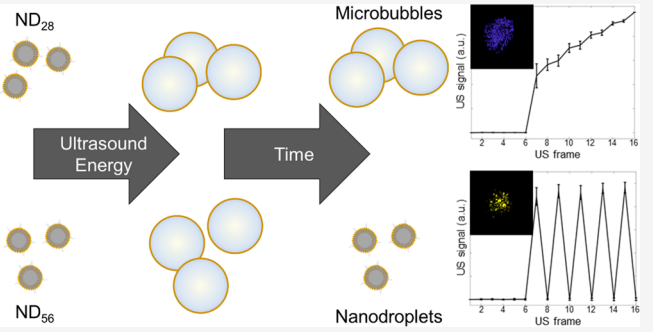

KEYWORDS: *perfluorocarbon nanodroplets, ultrasound, molecular imaging, multiplex imaging, acoustic droplet vaporization*

Molecular imaging harnesses targeted contrast agents to provide cell- or molecule-specific contrast.[1] The ability to noninvasively image molecular information has promise to enable the precise application of highly specific therapeutics. Several molecular imaging techniques have been developed and applied in preclinical and clinical applications, including positron emission tomography,[2] fluorescence imaging,[3] magnetic resonance imaging,[4] photoacoustic imaging,[5] and ultrasound (US) imaging.[6]

Ultrasound imaging has the benefit of being a real-time, nonionizing, and inexpensive imaging modality. Gaseous microbubbles are commonly used as contrast agents for US imaging.[6] The microbubbles typically contain a gaseous perfluorocarbon or oxygen core and a protein or lipid stabilizing shell. Importantly, the microbubbles generate excellent ultrasound contrast; single-microbubble sensitivity can be achieved. This has led to the development of novel imaging techniques, such as superlocalization US imaging.[7] Targeting molecules, such as antibodies, can be attached to the surface to confer molecular specificity. Various biological targets, including the vascular endothelial growth factor receptor and the $\alpha_v\beta_3$ integrin have been successfully imaged with US.[8] In spite of the strengths of microbubbles, their large size (typically 1 to 5 μm in diameter) restricts their applicability to intravascular targets. In addition, the relatively low stability of microbubbles limits their lifetime in circulation to a few minutes.[9]

Perfluorocarbon (PFC) nanodroplets have emerged as a promising alternative to microbubbles.[10,11] They contain a liquid (rather than gaseous) PFC core. Because liquid PFCs have acoustic properties similar to those of tissue, they provide negligible inherent contrast. They can, however, be activated by a burst of acoustic or optical energy to undergo a liquid-to-gas phase transition, a process known as acoustic droplet vaporization (ADV)[12] or optical droplet vaporization (ODV),[13] respectively. The resulting gaseous bubbles can be detected with US imaging with single bubble sensitivity. Depending on the ambient temperature and the boiling point of the PFC, the bubbles will either persist (low boiling point) or recondense back into their nanodroplet form (high boiling point), primed to undergo another vaporization event.[14−16]

Nanodroplets have many strengths over their microbubble counterparts. First, their small size and liquid core make them more stable in biological conditions and more likely to reach extravascular targets.[17] Second, they can be activated on-demand with externally applied energy.[18] This gives an extra level of control that can be leveraged to boost US contrast.[14]

Received: September 27, 2023
Revised: December 20, 2023
Accepted: December 21, 2023

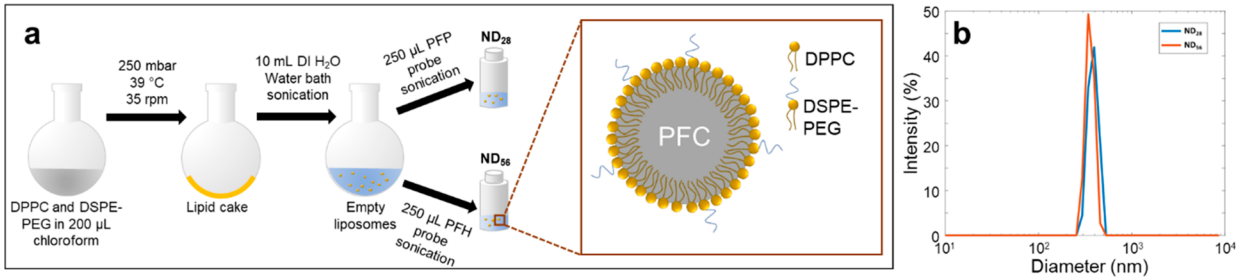

Figure 1. a) The synthesis procedure of ND_{28} and ND_{56} relied on sonication to generate a perfluorocarbon-in-water emulsion, with phospholipids forming the stabilizing shell. b) A histogram of the hydrodynamic diameter showed an average peak of 340 ± 43 nm for the ND_{28} and 350 ± 47 nm for the ND_{56}.

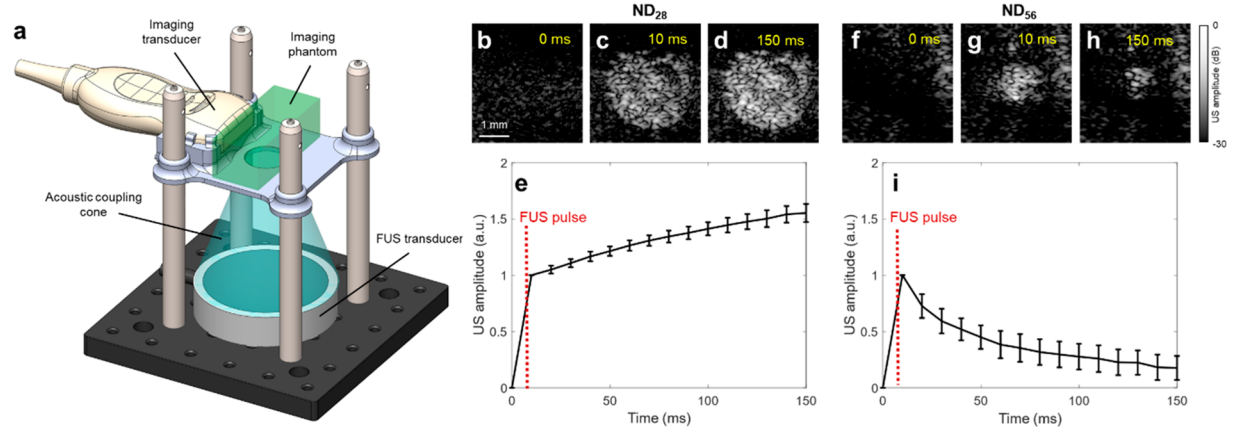

Figure 2. a) The experimental setup allowed for colocalized FUS focus and imaging field of view. Ultrasound images of polyacrylamide phantoms containing ND_{28} at b) 0 ms, c) 10 ms, and d) 150 ms show a sustained increase in signal in response to an FUS pulse applied just before 10 ms. e) The US signal amplitude shows consistent behavior across 8 acquisitions. Ultrasound images of polyacrylamide phantoms containing ND_{56} at f) 0 ms, g) 10 ms, and h) 150 ms show an initial increase in signal in response to the FUS pulse, followed by a gradual decay. i) The US signal amplitude shows consistent behavior across n = 8 acquisitions. Error bars represent the standard deviation.

Third, they can be loaded with optical dyes, nanoparticles, or therapeutic molecules for multimodal imaging or image-guided drug delivery.[13,19−21]

Multiplex imaging (the ability to detect and distinguish between two different formulations of contrast agents in the same imaging volume) expands the utility of molecular imaging to simultaneously visualize two markers or to control for nonspecific accumulation and binding.[22,23] Multiplex US imaging has proven to be elusive thus far. In theory, the resonant frequency of microbubbles could be tuned by varying their size and shell composition.[24] In practice, the polydispersity in their size makes it difficult to achieve two distinct populations of microbubbles. Alternatively, optical absorbers with distinct absorption spectra have been loaded in PFC nanodroplets.[25] Then, a tunable laser can be used to activate only a single population of nanodroplets at a time. The high attenuation of light in tissue, however, limits the imaging depth that can be achieved.

In this Letter, we describe a new approach to multiplex US imaging. We synthesized two formulations of PFC nanodroplets: one with a perfluoropentane core (bulk boiling point = 28 °C) and the other with a perfluorohexane core (boiling point = 56 °C). Both populations of nanodroplets can be vaporized with the same pulse of focused ultrasound (FUS) energy. When the ambient temperature is 37 °C, the perfluoropentane nanodroplets (ND_{28}) undergo a single vaporization event, whereas the perfluorohexane nanodroplets (ND_{56}) recondense after forming a transient bubble.[16] This distinct behavior was harnessed to develop an imaging strategy that can effectively differentiate between the two populations of nanodroplets. This work demonstrates that the relative ratio of the concentrations of ND_{28} and ND_{56} can be imaged. Overall, this approach could be applied to enable US imaging of multiple biomarkers in the same imaging volume.

The perfluorocarbon nanodroplets were synthesized (Figure 1a) by first forming a lipid cake from a solution containing a mixture of 1,2-dipalmitoyl-*sn*-glycero-3-phosphocholine (DPPC) and 1,2-distearoyl-*sn*-glycero-3-phosphoethanolamine-*N*-[(polyethylene glycol)-2000] (DSPE-PEG) in chloroform with a 90:10 weight ratio using a rotary evaporator. The lipids were rehydrated with deionized water and dispersed with a water bath sonicator. Then, either perfluoropentane or perfluorohexane was added, and a microtip probe sonicator was applied to produce ND_{28} or ND_{56}, respectively. Excess lipids were removed via centrifugation washing.

The nanodroplet size was measured via dynamic light scattering (DLS, Figure 1b). The ND_{28} had an average peak diameter of 340 ± 43 nm; ND_{56} had an average peak diameter of 350 ± 47 nm. The polydispersity index of the nanodroplets was 0.30 ± 0.11 and 0.27 ± 0.07 for ND_{28} and ND_{56}, respectively. The DLS instrument estimated the concentrations of the two samples to be 2.4×10^8 ND_{28}/mL and 2.1×10^8 ND_{56}/mL.

A custom imaging setup was designed that incorporates a 15 MHz linear array ultrasound imaging transducer and a 1.1-MHz single-element focused ultrasound (FUS) transducer

https://doi.org/10.1021/acs.nanolett.3c03719
Nano Lett. XXXX, XXX, XXX−XXX

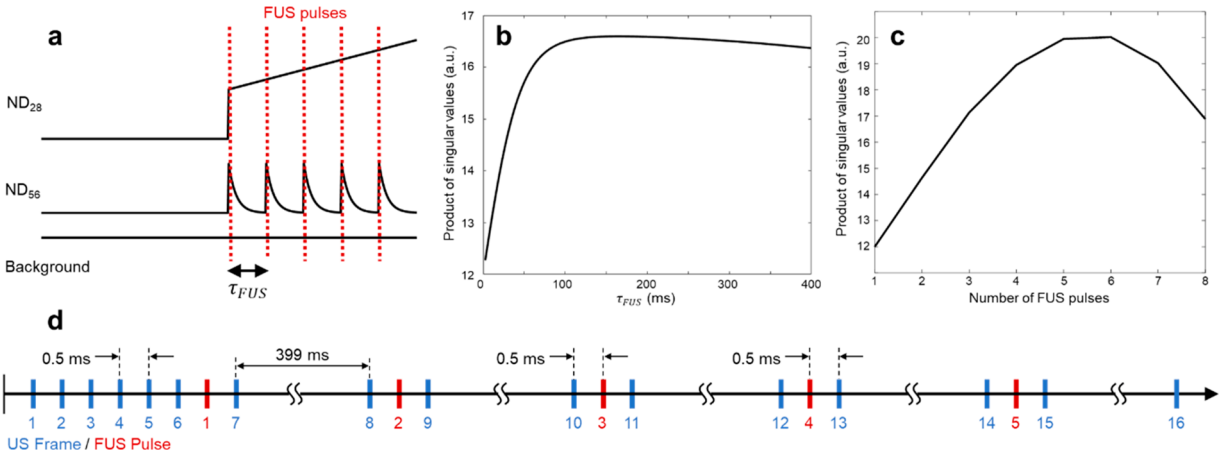

Figure 3. a) Simulated time traces for ND_{28} (top), ND_{56} (middle), and background (bottom). The number and spacing of FUS pulses were tuned to maximize the orthogonality of the three signals. The product of singular values was used as a metric to evaluate the relative differentiability of ND and background signal with respect to b) the spacing between FUS pulses τ_{FUS}, and c) the number of FUS pulses. d) Based on the results from (a,b), an image acquisition strategy consisting of 6 baseline frames and 5 FUS pulses was designed for multiplex imaging.

(Figure 2a). The imaging transducer was aligned with the focus of the FUS transducer by using a 3-D printed stage. The FUS transducer was coupled to the sample with a custom-molded polyacrylamide coupling cone with an ultrasound gel applied to all interfaces. A polyacrylamide gel phantom containing a homogeneous mixture of nanodroplets was used as the imaging medium. The FUS and imaging transducers were triggered by a function generator to allow submicrosecond synchronization between the FUS transmission and US image acquisition.

Three polyacrylamide phantoms containing a homogeneous distribution of either ND_{28} or ND_{56} were constructed with a concentration of 1.0×10^6 nanodroplets/mL. The phantoms were imaged to measure the temporal dynamics of the US signal in response to the FUS activation. An initial increase in ultrasound signal was observed for both ND_{28} and ND_{56} in response to the 1.1 MHz, 10-cycle FUS stimulus (Figure 2b–i). In the ensuing US frames, however, the intensity of the ND_{28} signal gradually increased (Figure 2b–e), while the intensity of the ND_{56} signal decayed back to the baseline (Figure 2f–i). The increasing ND_{28} signal is likely attributable to coalescence of the resulting bubbles, which are less stable than the nanodroplets, because of their larger surface area. This results in a lower stabilizing Laplace pressure and poorer lipid coverage.[26] It is also possible that the gaseous microbubbles harvest the PFC from nearby liquid nanodroplets, a phenomenon that has recently been demonstrated.[27] The decaying ND_{56} signal is attributable to the recondensation of the nanodroplets after their initial vaporization.[14−16] Our group has previously shown that ND_{56} can be revaporized hundreds to thousands of times with repeated FUS stimuli.[16]

The US images of ND_{28} and ND_{56} (Figure 2) demonstrated that the two populations of nanodroplets can exhibit distinct temporal behavior in response to a FUS stimulus. Leveraging these unique responses, an image acquisition strategy was developed to differentiate relative concentrations of mixed ND_{28}, ND_{56}, and background tissue signals. In order to do so, a matrix with three rows was constructed; each row contained the characteristic dynamic responses of ND_{28}, ND_{56}, and background tissue to FUS stimuli (Figure 3a). The number and spacing of FUS pulses were varied and the product of the singular values of the matrix containing the idealized signals was used as a metric for its invertibility and, thus, the differentiability of the three signals. The product of singular values was maximized for a longer delay between FUS pulses, τ_{FUS} (Figure 3b). This allowed for the ND_{56} to decay to a near baseline signal before a new vaporization pulse was applied. In addition, increasing the number of FUS pulses beyond 5 yielded diminishing returns (Figure 3c). Based on the results of this optimization, the image acquisition sequence that used a τ_{FUS} of 400 ms and 5 total FUS pulses was selected. It is noteworthy that this results in a relatively long image acquisition time of 2 s. This could result in errors arising from tissue motion in *in vivo* settings. It has been shown that exposure of ND_{56} to additional imaging pulses can hasten the recondensation process.[28] Future work will focus on minimizing the ND_{56} recondensation process for faster image acquisition.

Next, the number of US images needed was reduced as far as possible, while preserving the differentiability of the three signals. This was done using an algorithm adapted from our previous work in wavelength selection for spectroscopic photoacoustic imaging.[29] Briefly, a single column (representing a single US frame) was removed from the matrix containing the three signals. Then, the product of the singular values was calculated. This was repeated for each possible frame. The frame that led to the largest product of singular values when removed was deemed to be the least important and discarded. The process was repeated until only 16 US frames remained. This led to the image acquisition strategy shown in Figure 3d. First, 6 baseline frames were acquired, then 5 FUS pulses were applied, with a pair of US frames acquired 0.5 and 400 ms after each FUS pulse. This image acquisition sequence was used for all subsequent experiments.

Polyacrylamide phantoms containing a homogeneous distribution of either ND_{28} or ND_{56} were imaged using the developed imaging sequence. The concentrations of ND_{28} and ND_{56} were matched using DLS measurements. Representative images of the two populations of nanodroplets qualitatively demonstrated that they can be differentiable using the image acquisition strategy (Figure 4a,b). The images capture the strong one-time vaporization that ND_{28} exhibited in response to the first FUS pulse, followed by a gradual increase in signal. The ND_{56} exhibited a vaporization signal in response to each of the five FUS pulses, with recondensation occurring before

https://doi.org/10.1021/acs.nanolett.3c03719
Nano Lett. XXXX, XXX, XXX−XXX

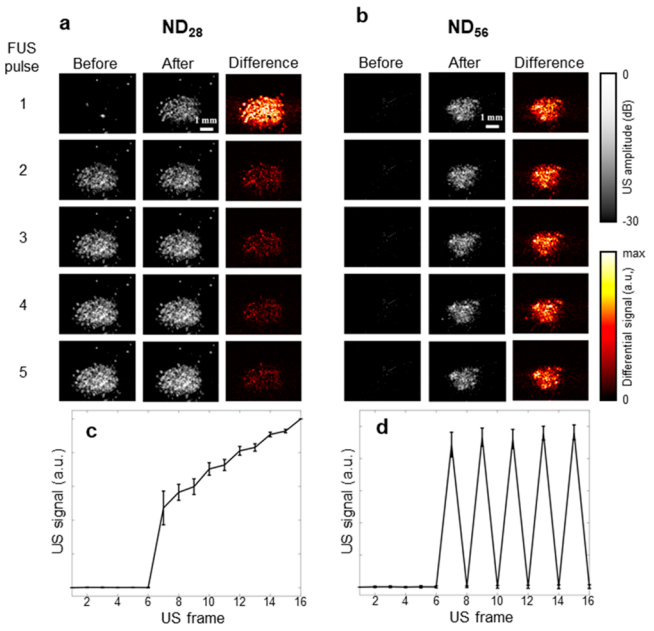

Figure 4. Representative US images of phantoms containing a) ND_{28} and b) ND_{56} before (left column) and 0.5 ms after (middle column) each of the 5 FUS pulses using the image acquisition strategy shown in Figure 3d. The difference image (right column) demonstrates a single large vaporization event for ND_{28} and multiple vaporization events for the ND_{56}. The signals were acquired from 7 phantoms, and the average US signal was plotted for c) ND_{28} and d) ND_{56}. The error bars represent one standard deviation.

each subsequent FUS pulse was applied. Images from 7 phantoms were acquired to obtain the ground-truth signals of ND_{28} and ND_{56} (Figure 4c,d) using the imaging sequence shown in Figure 3d. These signals were then used for multiplex imaging studies.

Polyacrylamide phantoms containing homogeneous mixtures of ND_{28} and ND_{56} with a relative percentage of ND_{56} ranging from 0% to 100% in 10% increments were constructed. Five locations in each phantom were imaged by using the developed imaging sequence (Figure 3d). The signals in a region of interest corresponding to the FUS focal spot were averaged for each US frame. Then, each of these 16-sample ultrasound amplitudes was unmixed using non-negative least-squares to obtain relative contributions of the ND_{28}, ND_{56}, and background to the US signal. Finally, the relative percentage of ND_{56} was calculated.

The resulting estimate of % of ND_{56} showed a good agreement with the ground truth (Figure 5a). The average error in the relative ND_{56} concentration was 9.1%, with larger errors occurring at higher ND_{56} concentrations. A linear regression demonstrated high linearity of the estimated relative concentration against the ground truth (R^2 = 0.996). It is important to note, however, that the slope of the line was 0.76, indicating an underestimation of ND_{56} in these samples. This discrepancy is likely attributable to the fact that the nanodroplet concentrations were measured using DLS, which is not the most accurate method for quantifying nanoparticle concentrations. In future studies, the concentration of the two nanodroplet populations could be matched using their US signal, enabling more accurate unmixing. In addition, imaging

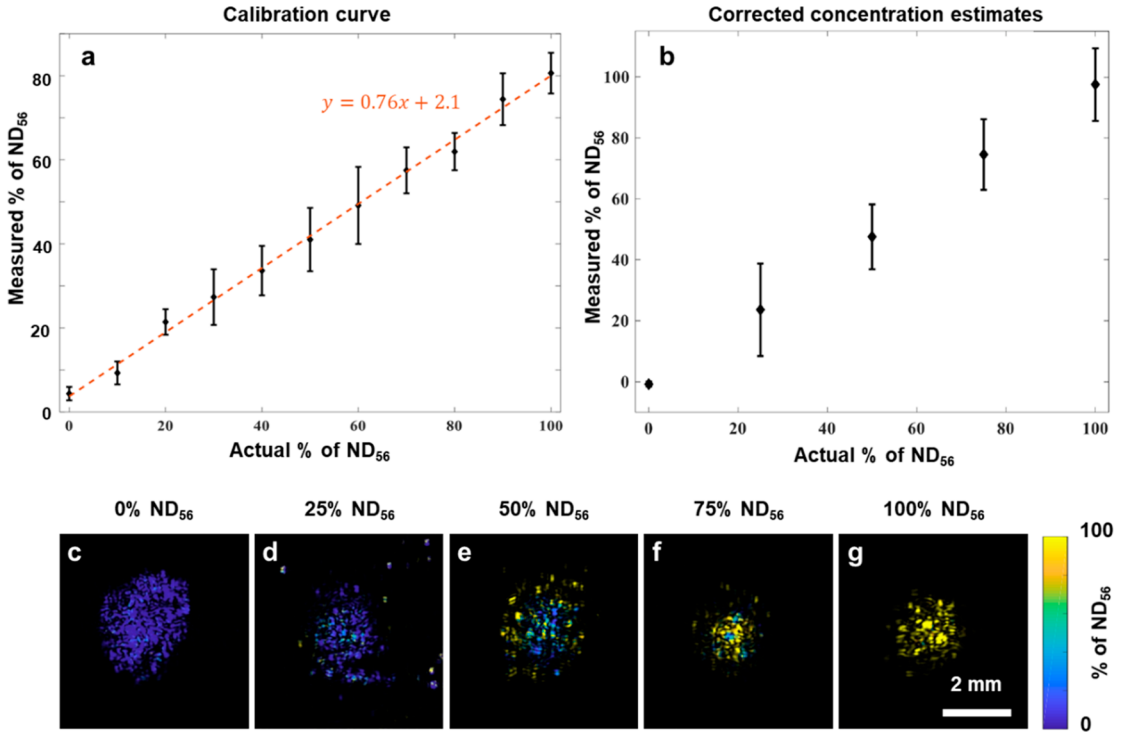

Figure 5. a) Average relative concentration of ND_{56} estimated from linear unmixing of the ND_{28}, ND_{56}, and background signals. Error bars indicate the standard deviation of 5 imaging locations in each of 3 phantoms at each concentration level. The red line indicates a linear fit (R^2 = 0.996). b) A separate set of phantoms was imaged using the linear fit from (a) as a correction, showing better agreement with the ground truth. Error bars represent the standard deviation of 5 imaging locations for a single phantom at each concentration. Representative images of the corrected unmixed signals show the spatial distribution of the ND_{28} (blue) and ND_{56} (yellow) for phantoms containing a relative concentration of c) 0%, d) 25%, e) 50%, f) 75%, and g) 100% ND_{56}.

https://doi.org/10.1021/acs.nanolett.3c03719
Nano Lett. XXXX, XXX, XXX−XXX

noise and artifacts arising from microbubble shadowing could have impacted the results.

In order to correct for the nonideal concentration estimate, the linear fit in Figure 5a was used as a calibration curve for a second set of experiments. Phantoms containing 0%, 25%, 50%, 75%, or 100% ND_{56} were imaged. The estimated concentrations were then scaled by a linear fit from the preceding experiment. The results demonstrated that a much better agreement between the actual and estimated relative ND_{56} concentration with an average error of 1.1%, (Figure 5b). In addition, since the processing was carried out in a pixelwise manner, images of ND_{28} and ND_{56} concentration can be obtained. Representative images of the relative ND_{56} concentration (Figure 5c–g) showed that the two populations of nanodroplets can be simultaneously visualized in the same imaging volume. This opens the door to visualizing multiple molecular targets simultaneously in the same imaging volume. It also allows for the possibility of using a nontargeted nanodroplet to help distinguish between contrast agent delivery and specific binding to the molecule of interest. This approach has been successfully applied in fluorescence imaging for highly sensitive detection of a molecule of interest.[30,31]

In this paper, a new multiplex ultrasound imaging strategy was described and initially tested, one that leverages the unique temporal dynamics of two populations of perfluorocarbon nanodroplets in response to the same FUS stimulus. The distinct behavior of the two populations was characterized and used to develop an image acquisition strategy designed to optimize the separation of ND signals. Finally, the ability to simultaneously visualize the two different nanodroplets in the same imaging volume was demonstrated by using tissue-mimicking phantoms. Future work will explore adding molecular targeting to the nanodroplets and applying the technique *in vivo*.

■ ASSOCIATED CONTENT

Supporting Information

The Supporting Information is available free of charge at https://pubs.acs.org/doi/10.1021/acs.nanolett.3c03719.

Descriptions of nanodroplet synthesis and characterization, tissue-mimicking phantom preparation, ultrasound activation and imaging, imaging sequence simulation and optimization, and multiplex imaging (PDF)

■ AUTHOR INFORMATION

Corresponding Author

Geoffrey P. Luke − *Thayer School of Engineering, Dartmouth College, Hanover, New Hampshire 03755, United States; Translational Engineering in Cancer Research Program, Dartmouth Cancer Center, Lebanon, New Hampshire 03766, United States;* orcid.org/0000-0002-1486-3398; Email: geoffrey.p.luke@dartmouth.edu

Authors

Austin Van Namen − *Thayer School of Engineering, Dartmouth College, Hanover, New Hampshire 03755, United States*

Sidhartha Jandhyala − *Thayer School of Engineering, Dartmouth College, Hanover, New Hampshire 03755, United States*

Catalina-Paula Spatarelu − *Thayer School of Engineering, Dartmouth College, Hanover, New Hampshire 03755, United States*

Kenneth M. Tichauer − *Biomedical Engineering, Illinois Institute of Technology, Chicago, Illinois 60616, United States*

Kimberley S. Samkoe − *Thayer School of Engineering, Dartmouth College, Hanover, New Hampshire 03755, United States; Translational Engineering in Cancer Research Program, Dartmouth Cancer Center, Lebanon, New Hampshire 03766, United States*

Complete contact information is available at: https://pubs.acs.org/10.1021/acs.nanolett.3c03719

Author Contributions

The manuscript was written through contributions of all authors. All authors have given approval to the final version of the manuscript.

Funding

This work was funded by the National Institutes of Health (R56DE033175) and a Prouty Pilot Grant from the Dartmouth Cancer Center.

Notes

The authors declare no competing financial interest.

■ ABBREVIATIONS

DLS, dynamic light scattering; DPPC, 1,2-dipalmitoyl-*sn*-glycero-3-phosphocholine; DSPE-PEG, 1,2-distearoyl-*sn*-glycero-3- phosphoethanolamine-*N*-(amino(polyethylene glycol)-2000); FUS, focused ultrasound; ND_{28}, perfluoropentane nanodroplets; ND_{56}, perfluorohexane nanodroplets; PFC, perfluorocarbon; US, ultrasound

■ REFERENCES

(1) Rowe, S. P.; Pomper, M. G. Molecular imaging in oncology: Current impact and future directions. *CA: a cancer journal for clinicians* **2022**, *72* (4), 333−352.

(2) Vaz, S. C.; Oliveira, F.; Herrmann, K.; Veit-Haibach, P. Nuclear medicine and molecular imaging advances in the 21st century. *British journal of radiology* **2020**, *93* (1110), 20200095.

(3) Cheng, P.; Pu, K. Molecular imaging and disease theranostics with renal-clearable optical agents. *Nature Reviews Materials* **2021**, *6* (12), 1095−1113.

(4) Li, H.; Meade, T. J. Molecular magnetic resonance imaging with Gd (III)-based contrast agents: challenges and key advances. *J. Am. Chem. Soc.* **2019**, *141* (43), 17025−17041.

(5) Yao, J.; Wang, L. V. Recent progress in photoacoustic molecular imaging. *Curr. Opin. Chem. Biol.* **2018**, *45*, 104−112.

(6) Abou-Elkacem, L.; Bachawal, S. V.; Willmann, J. K. Ultrasound molecular imaging: Moving toward clinical translation. *European journal of radiology* **2015**, *84* (9), 1685−1693.

(7) Errico, C.; Pierre, J.; Pezet, S.; Desailly, Y.; Lenkei, Z.; Couture, O.; Tanter, M. Ultrafast ultrasound localization microscopy for deep super-resolution vascular imaging. *Nature* **2015**, *527* (7579), 499.

(8) Willmann, J. K.; Lutz, A. M.; Paulmurugan, R.; Patel, M. R.; Chu, P.; Rosenberg, J.; Gambhir, S. S. Dual-targeted contrast agent for US assessment of tumor angiogenesis in vivo. *Radiology* **2008**, *248* (3), 936−944.

(9) Mullin, L.; Gessner, R.; Kwan, J.; Kaya, M.; Borden, M. A.; Dayton, P. A. Effect of anesthesia carrier gas on in vivo circulation times of ultrasound microbubble contrast agents in rats. *Contrast media & molecular imaging* **2011**, *6* (3), 126−131.

(10) Guo, R.; Xu, N.; Liu, Y.; Ling, G.; Yu, J.; Zhang, P. Functional ultrasound-triggered phase-shift perfluorocarbon nanodroplets for

cancer therapy. *Ultrasound in Medicine & Biology* **2021**, *47* (8), 2064–2079.
(11) Yoon, H. Ultrasound and Photoacoustic Imaging of Laser-Activated Phase-Change Perfluorocarbon Nanodroplets. *Photonics* **2021**, *8*, 405.
(12) Zhou, Y. Application of acoustic droplet vaporization in ultrasound therapy. *Journal of therapeutic ultrasound* **2015**, *3* (1), 20.
(13) Wilson, K.; Homan, K.; Emelianov, S. Biomedical photoacoustics beyond thermal expansion using triggered nanodroplet vaporization for contrast-enhanced imaging. *Nat. Commun.* **2012**, *3*, 618.
(14) Hannah, A. S.; Luke, G. P.; Emelianov, S. Y. Blinking phase-change nanocapsules enable background-free ultrasound imaging. *Theranostics* **2016**, *6* (11), 1866.
(15) Luke, G. P.; Hannah, A. S.; Emelianov, S. Y. Super-resolution ultrasound imaging in vivo with transient laser-activated nanodroplets. *Nano Lett.* **2016**, *16* (4), 2556–2559.
(16) Van Namen, A.; Jandhyala, S.; Jordan, T.; Luke, G. P. Repeated Acoustic Vaporization of Perfluorohexane Nanodroplets for Contrast-Enhanced Ultrasound Imaging. *IEEE Transactions on Ultrasonics, Ferroelectrics, and Frequency Control* **2021**, *68* (12), 3497–3506.
(17) Rapoport, N. Drug-loaded perfluorocarbon nanodroplets for ultrasound-mediated drug delivery. *Therapeutic ultrasound* **2016**, *880*, 221–241.
(18) Dayton, P. A.; Zhao, S.; Bloch, S. H.; Schumann, P.; Penrose, K.; Matsunaga, T. O.; Zutshi, R.; Doinikov, A.; Ferrara, K. W. Application of ultrasound to selectively localize nanodroplets for targeted imaging and therapy. *Molecular imaging* **2006**, *5* (3), 7290.2006. 00019.
(19) Santiesteban, D. Y.; Dumani, D. S.; Profili, D.; Emelianov, S. Y. Copper sulfide perfluorocarbon nanodroplets as clinically relevant photoacoustic/ultrasound imaging agents. *Nano Lett.* **2017**, *17* (10), 5984–5989.
(20) Spatarelu, C.-P.; Jandhyala, S.; Luke, G. P. Dual-drug Loaded Ultrasound-responsive Nanodroplets for On-demand Combination Chemotherapy. *Ultrasonics* **2023**, *133*, 107056.
(21) Spatarelu, C.-P.; Van Namen, A.; Jandhyala, S.; Luke, G. P. Fluorescent Phase-Changing Perfluorocarbon Nanodroplets as Activatable Near-Infrared Probes. *International Journal of Molecular Sciences* **2022**, *23* (13), 7312.
(22) Andreou, C.; Weissleder, R.; Kircher, M. F. Multiplexed imaging in oncology. *Nature Biomedical Engineering* **2022**, *6* (5), 527–540.
(23) Heinzmann, K.; Carter, L. M.; Lewis, J. S.; Aboagye, E. O. Multiplexed imaging for diagnosis and therapy. *Nature Biomedical Engineering* **2017**, *1* (9), 697–713.
(24) Van der Meer, S. M.; Dollet, B.; Voormolen, M. M.; Chin, C. T.; Bouakaz, A.; de Jong, N.; Versluis, M.; Lohse, D. Microbubble spectroscopy of ultrasound contrast agents. *J. Acoust. Soc. Am.* **2007**, *121* (1), 648–656.
(25) Santiesteban, D. Y.; Hallam, K. A.; Yarmoska, S. K.; Emelianov, S. Y. Color-coded perfluorocarbon nanodroplets for multiplexed ultrasound and photoacoustic imaging. *Nano research* **2019**, *12*, 741–747.
(26) Kwan, J. J.; Borden, M. A. Lipid monolayer collapse and microbubble stability. *Advances in colloid and interface science* **2012**, *183*, 82–99.
(27) Brambila, C. J.; Lux, J.; Mattrey, R. F.; Boyd, D.; Borden, M. A.; de Gracia Lux, C. Bubble inflation using phase-change perfluorocarbon nanodroplets as a strategy for enhanced ultrasound imaging and therapy. *Langmuir* **2020**, *36* (11), 2954–2965.
(28) Zhu, Y. I.; Yoon, H.; Zhao, A. X.; Emelianov, S. Y. Leveraging the imaging transmit pulse to manipulate phase-change nanodroplets for contrast-enhanced ultrasound. *IEEE transactions on ultrasonics, ferroelectrics, and frequency control* **2019**, *66* (4), 692–700.
(29) Luke, G. P.; Emelianov, S. Y. Optimization of in vivo spectroscopic photoacoustic imaging by smart optical wavelength selection. *Optics letters* **2014**, *39* (7), 2214–2217.
(30) Tichauer, K. M.; Samkoe, K. S.; Gunn, J. R.; Kanick, S. C.; Hoopes, P. J.; Barth, R. J.; Kaufman, P. A.; Hasan, T.; Pogue, B. W. Microscopic lymph node tumor burden quantified by macroscopic dual-tracer molecular imaging. *Nature medicine* **2014**, *20* (11), 1348.
(31) Wang, C.; Folaron, M.; Gunn, J.; Hodge, S.; Chen, E.; Hoopes, P. J.; Tichauer, K.; Samkoe, K. Improved Tumor Discrimination and Shortened Administration-to-Imaging Times in Fluorescence Guided Surgery Through Paired-Agent Protocols. *Mol Imaging Biol* **2023**, *25*, 110.

https://doi.org/10.1021/acs.nanolett.3c03719
Nano Lett. XXXX, XXX, XXX–XXX